PAPER Nr. : 3

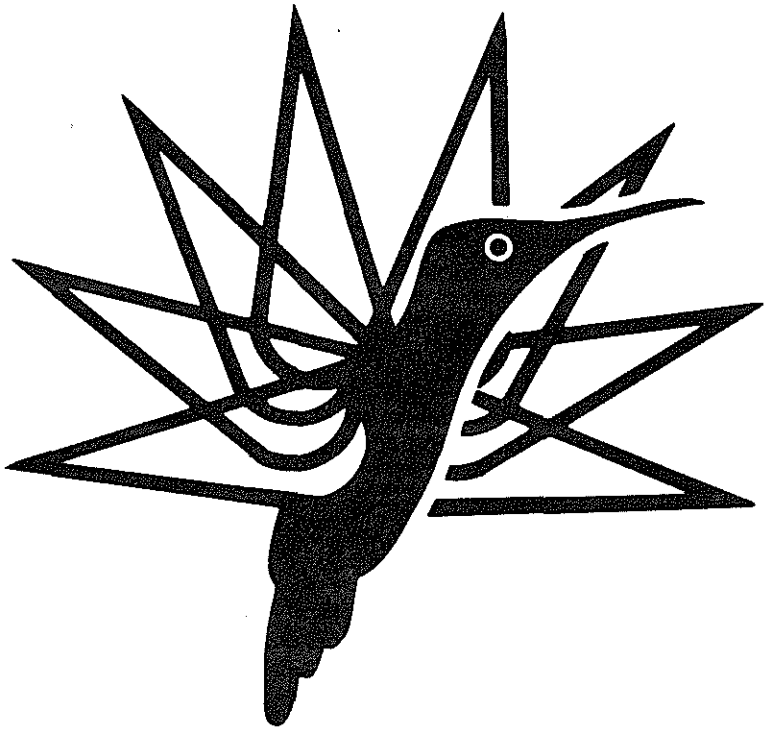

APPLICATIONS OF AN ANALYSIS OF AXISYMMETRIC BODY EFFECTS ON ROTOR PERFORMANCE AND LOADS

BY

W. JOHNSON AND G. K. YAMAUCHI

NASA AMES RESEARCH CENTER
MOFFETT FIELD, CALIFORNIA, U.S.A.

TENTH EUROPEAN ROTORCRAFT FORUM

AUGUST 28 – 31, 1984 – THE HAGUE, THE NETHERLANDS

APPLICATIONS OF AN ANALYSIS OF AXISYMMETRIC BODY EFFECTS ON ROTOR PERFORMANCE AND LOADS

Wayne Johnson and G. K. Yamauchi

NASA Ames Research Center
Moffett Field, California 94035 U.S.A.

Abstract

A computationally efficient body analysis is developed and coupled with a comprehensive helicopter analysis to calculate the body-induced aerodynamic effects on rotor performance and loads. A modified slender-body theory is used as the body model. With the objective of demonstrating the accuracy, efficiency, and application of the method, the analysis at this stage is restricted to axisymmetric bodies at zero angle of attack. By comparing with results from an exact analysis for simple body shapes, it is found that the modified slender body theory provides an accurate potential flow solution for moderately thick bodies, with only a 10%-20% increase in computational effort over that of an isolated rotor analysis. The computational ease of this method provides a means for routine assessment of body-induced effects on a rotor. Results are given for several configurations that typify those being used in the Ames 40- by 80-Foot Wind Tunnel and in the rotor-body interference tests being conducted at Ames.

Symbols

$\bar{c}$	blade mean chord, $\pi\sigma R/N$
C_{m_x}	blade flapwise bending moment divided by $\rho\Omega^2R^4\bar{c}$
C_{m_z}	blade edgewise bending moment divided by $\rho\Omega^2R^4\bar{c}$
C_T	rotor thrust divided by $\rho(\Omega R)^2\pi R^2$
ℓ	body length
L/D	rotor lift-to-drag ratio = (lift*speed)/(power + drag*speed)
N	number of blades
q	strength of axial source distribution
R	rotor radius
t	maximum thickness of body (measured from body centerline)
U	free-stream velocity
x,y,z	coordinate system with origin at body nose; x positive aft, y positive to right, z positive upward

α_S shaft angle, positive aft

α_{TPP} tip-path-plane angle of attack, positive aft

μ advance ratio, $U/\Omega R$

ξ axial coordinate of source distribution

ρ air density

σ rotor solidity (total blade area divided by disk area)

ψ rotor blade azimuth position

Ω rotor rotational speed

1. Introduction

The aerodynamic interaction between the rotor and the fuselage of a helicopter has been shown experimentally to have significant effects (e.g., in Refs. [1] and [2]). Ideally, analytical models of the rotor-induced effects at the body and the body-induced effects at the rotor need to be combined. The end result of such a combination, however, would require the coupling of complex body and rotor computer codes to calculate the system behavior. Typical past efforts (Refs. [3] and [4]) have coupled potential flow panel methods for fuselage aerodynamic analysis with simplified rotor analytical models. For investigations emphasizing the rotor, an efficient analytical model for the fuselage is desirable, rather than a complex and time-consuming paneling code. This report presents the development of an efficient body model using a modified slender body theory to calculate the flow field of an axisymmetric body at zero angle of attack. The present investigation will ultimately lead to a general model for the body shape and will include flows at nonzero angle of attack. The body analysis is coupled with a comprehensive helicopter analysis (Ref. [5]) to calculate the body-induced effects on rotor performance and loads. The approach is verified by comparing the results for performance and loads from the modified slender body theory with results from an exact analysis for simple shapes. Next, the body-induced effects on the rotor are calculated for several realistic cases: a typical full-scale rotor test configuration, and configurations representing the model and the full-scale aerodynamic interference tests at Ames. Finally, the efficiency of the modified slender body theory computations is discussed.

2. Background on Rotor-Body Interaction

Body-induced effects on the rotor have received somewhat less attention than rotor-induced effects on the body (Refs. [2]-[4] and [6]-[15]). Reference [4] provides a summary of some of the analytical work done in the rotor-body interaction area. References [2], [4], and [10]-[13] include calculations of body-induced effects on helicopter rotors; Refs. [3], [6], [9], [14], and [15] provide experimental data.

Ames Research Center is engaged in an experimental program to measure the aerodynamic interaction between the rotor and fuselage. Several small-scale tests have been completed (Refs. [6]-[9]), and more are planned; full-scale tests will be conducted in the future. For the baseline fuselage bodies, these investigations use axisymmetric shapes. Hence, although the present analytical investigation is restricted to axisymmetric shapes for the purpose of demonstrating its accuracy and limits, the method is directly applicable to the configurations of this experimental program. The two test modules routinely used for full-scale rotor tests in the Ames 40- by 80-Foot Wind Tunnel — the Rotor Test Apparatus (RTA) and the Easter Egg (EE) — provide body shapes for calculating rotor performance and loads. Figure 1 shows a model rotor and 1/6-scale models of these two test modules in the Ames 7- by 10-Foot Wind Tunnel for aerodynamic interference tests. Figure 2 shows a typical full-scale rotor on the RTA in the 40- by 80-Foot Wind Tunnel. Reference [6] presents the experimental effects of a body of revolution on rotor performance. Advance ratio, tip-path-plane angle, body angle, rotor-body separation, and hub position are varied. In Ref. [7], however, it was concluded that the rotor data obtained in Ref. [6] were not accurate enough for making conclusions about the influence of the body on rotor performance. Reference [9] gives data for bodies modeling the future full-scale test, but again the rotor performance data are not accurate enough to assess the influence of the body (due to hub tares).

3. Development of Theory

In developing an analytical model for the body flow field, the primary consideration was the computational efficiency of the method. The calculation of isolated rotor performance and loads is already a computationally expensive task. If the combined rotor-body behavior is to be predicted for routine use, it must require the same order of computer time as the isolated rotor problem. A number of panel methods have been developed for calculating the flow field of arbitrary bodies. These methods typically require several times the computer time of the rotor analysis; hence, their usefulness is limited. A more efficient method is thus required. Considering the sources of the large computation time required for the panel codes, the conclusion is made that an efficient technique must use on the order of 100 singularities, and must obtain the singularity strength directly from the body shape (without inversion or iteration steps). Slender body theory, using small integration steps to evaluate the body-induced velocities, satisfies these requirements. For the cases considered here (axisymmetric bodies at zero angle of attack), the development of a surface singularity method that would be reasonably efficient is possible. Unlike slender body theory, however, such a technique would not retain its efficiency when extended to the more general problem. Full details of the development and implementation of the theory are given in Ref. [16].

The basis for the body model is slender body theory; potential flow is assumed. Since axisymmetric bodies are assumed, the stream function of an axial source distribution is used (Ref. [17]). The flow field is represented by sources (with strength q) distributed along

the axis. The slender body theory result is

$$q_{SB}(\xi) = UA'(\xi) = U2\pi r_o(\xi)r_o'(\xi)$$

where $A = \pi r_o^2$ is the cross-sectional area of the body and U is the free-stream velocity (see Ref. [17] for details).

Ideally, the stagnation points of the flow field are located at the nose and at the tail of the body. For bodies with blunt noses and tails, the stagnation points will be forward of the nose and aft of the tail, if the source distribution is allowed to run from the nose to the tail. The amount of overshoot of the stagnation point varies from 1% to 13% of the body length for ellipsoids with maximum thicknesses of $t = 0.1$ to 0.5. To correct for this overshoot, the limits of integration were modified. For bodies with blunt ends, Ref. [18] shows that good approximations for the locations of the limits of integration are points that are halfway between the nose and the center of curvature of the nose (RCN), and halfway between the tail and the center of curvature of the tail (RCT).

For moderately thick bodies, slender body theory underpredicts the maximum thickness. For bodies that are symmetric fore and aft, such as ellipsoids, a factor of K is all that is needed to match the maximum thickness. As a result, for ellipsoids, the source strength used was $q = Kq_{SB}(\xi)$. The amount of stagnation point overshoot is reduced by using the modified theory. For ellipsoids with maximum thicknesses from $t = 0.1$ to $t = 0.5$, the overshoot ranged from 0.05% to 6% (with the maximum thickness matched exactly).

For the case of more general bodies that are not symmetric fore and aft, a compressed coordinate system was introduced to maintain net zero source strength: $\xi^* = (\xi - RCN/2)/(1 - RCA)$ where $RCA = (RCN + RCT)/2$. Results then obtained for the zero streamline show that the nose is well-modeled, but that a pointed tail is not. Regular slender-body theory, however, models the tail shape well, but it breaks down near the nose. An additional condition was therefore needed to improve the mathematical model; that is, the derivative of the singularity strength at a pointed nose or tail was maintained in order to match the body slope. Thus, let q take on the following form:

$$q(\xi) = \mathcal{K}q_{SB}(\xi^*) + f(\xi^*)(\xi^* - 1)(1 - \mathcal{K}\xi^{*\prime})q_{SB}'(1)$$

where $\mathcal{K}$ is a factor such that the point of maximum thickness is matched. Note that $q'(1) = q_{SB}'(1)$ if $f(1) = 1/\xi^{*\prime}$. For a closed body, the net source strength must be zero. In addition, the condition of $f(0) = 0$ must be met to maintain the source distribution at the nose. It was also desired that f be a continuous function to prevent difficulties in the numerical integration scheme. A piecewise linear function satisfying these criteria was used (see Ref. [16]). This function has two free parameters, which are determined by trial and error for a given body shape. The tail correction procedure may be difficult to generalize to other body shapes, especially those with

abrupt changes in body slopes. Several attempts were necessary to choose the values of the two free parameters for the cases in this report.

The EE and the RTA test modules have blunt ends; however, the radii of curvature of the tails are very small relative to the body lengths (see Fig. 3). To apply the modified slender body theory with tail correction, the tails of the EE and RTA were extended to a point. The extension increased the length of the EE by about 7.7%; the RTA length increased by 9.9%. The tail extension is a more accurate model of the body end, considering the physical behavior of the flow in this region.

Exact solutions describing the flow about a sphere or an ellipsoid can be found in the fluid mechanics literature (Ref. [19], for example). Equations for the exact velocity solutions used in this paper are derived in Ref. [16].

After the satisfactory development of the various body models, the next step was to introduce the body-induced velocities into the comprehensive helicopter analysis (CAMRAD) (Ref. [5]). The solution procedure for the rotor behavior is basically unchanged, since no iteration between the body and rotor is involved (except to update the body-induced velocities when the rotor position relative to the body changes as the trim iteration proceeds). The body-induced velocities are calculated for each location on the rotor disk. The location on the rotor disk where the body-induced velocities are calculated depends on the blade motion; therefore, ideally the induced velocities should be calculated at least once per circulation iteration within CAMRAD. However, this resulted in a large number of induced velocity calculations which were unnecessary in achieving convergence. Calculating the induced velocities once per control iteration was more than sufficient, since the rotor position changes little during the final stages of the trim iteration, as shown in Fig. 4, for a representative forward flight analysis.

4. Analytical Model of Rotor

Three types of rotors (Table 1) were used in the present study. Nonuniform inflow and a free-wake geometry (for two or three revolutions of the wake) were used to model the rotor environment. Results obtained from use of a prescribed wake geometry showed no significant change from the free-wake results. For rotor A, a teetering flap mode with one harmonic of motion was used. For rotors B and C, six flap/lag bending modes (including the rigid body modes) and one blade pitch mode were used; seven harmonics of motion were used for each mode. Rotor A is a stiff model rotor, for which only the performance was calculated. Both rotor performance and loads were calculated for rotors B and C. All the calculations were performed for sea level standard conditions. The rotor tip Mach number was held constant, and the advance ratio was in the range $\mu = 0.15$ to 0.50. The rotor thrust and the tip-path-plane tilt relative to the rotor shaft were trimmed to specified values by varying the rotor collective pitch and cyclic pitch control angles. The body velocities were recalculated after each control change during

the rotor trim iteration, ensuring that the velocities were evaluated at the correct rotor position.

The adequacy of the rotor model was assessed by comparing the theory with experimental rotor data. For the L/D as a function of thrust over a range of advance ratios, the correlation was good. For the one-half peak-to-peak blade loads versus advance ratio, the correlation was good to fair; similar correlation is shown in Ref. [13]. Figure 5 shows the surface pressure distribution on a 1/6-scale EE, obtained from Ref. [8], compared with the distribution calculated by the modified slender-body theory with tail correction. The theory compares well with the data and with the panel code from Ref. [8], except for $x \gtrsim 0.95$. An explanation for the lack of agreement in this vicinity is that the data represent the occurrence of flow separation. The theory, at this stage of development, does not model separation. The influence of the rotor on the body pressure is greater than the error caused by separation at the tail (see Ref. [8]).

The changes in blade loads and profile power are due to changes in the complex flow field of the rotor blade. The body velocities do not simply produce an incremental change in blade loads and power. Because of the nonlinear relationship between the perturbation velocities and the blade loads and the profile power, proper calculation of the blade angle of attack distribution is necessary. Changes in the induced power caused by the body would be zero if a uniform inflow model (momentum theory with empirical corrections) was used. Even the direct interference power requires a detailed thrust distribution over the rotor disk. Hence, a nonuniform inflow model is necessary to assess body-induced effects on rotor behavior. A free-wake geometry was used for all calculations presented in this paper. Comparisons were made with prescribed wake results, and no significant changes were found in performance or loads caused by the wake distortion. Hence, the body-induced wake geometry variations would not be important either. The absence of the distortion of the wake geometry by the body in the present analysis, therefore, is not significant. The change in the body flow field due to the rotor, which then changes the perturbation velocities at the rotor, is also neglected.

5. Results: Verification of Approach

The accuracy of the modified slender body theory will be examined for case 1 of Table 2: ellipsoids and axisymmetric bodies with a NACA four-digit airfoil thickness distribution. The ellipsoid case is useful because the exact solution for the body-induced velocities is known. The airfoil shapes are a reasonable approximation for typical wind-tunnel test modules. The complete modified slender body theory with tail correction will serve as the "exact" solution for the airfoil shaped bodies.

Figure 6 shows the dividing streamline (body shape) of ellipsoids, as obtained by unmodified and modified slender body theory. Compared with the exact body shape, the modified theory shows good accuracy for the 60%-thick body, and fair accuracy for the 80%-thick body. Calculations of the flow field (velocity magnitude and angle of

attack) were made for 60%-, 80%-, and 100%-thick ellipsoids in planes above the bodies. Relative to the exact solution, slender body theory showed significant errors for all three bodies. The modified theory predicted both the velocity magnitude and the angle of attack well, even though the body shapes were not matched exactly (Fig. 6). For the section angle of attack changes induced by the body on a rotor blade, the modified slender body theory results were again almost identical to those of the exact solution for the 60%- and the 80%-thick bodies.

Figure 7 shows axisymmetric bodies with a NACA four-digit airfoil thickness distribution. Results are shown from the modified theory with and without the tail correction. The full, modified slender-body theory gives good results. The angle of attack change at the rotor blade for a 30%-thick airfoil shape was calculated. Since slender body theory models the shape of the tail correctly, aft of the hub position (which was located above the body 0.3-chord station) the slender body theory was actually closer to the exact solution (represented by the full modified theory) than was the modified theory without tail correction. Forward of the hub position, the modified theory without tail correction and slender body theory solutions were similar. Hence the theory without the tail correction was in error both forward and aft of the hub.

After satisfactory modeling of the ellipsoids and airfoils had been achieved, the next step was to determine the difference in rotor performance and loads as calculated using modified slender body theory and the exact solution (for airfoil shapes, the modified slender body theory with tail correction results served as the "exact" solution). All values in this paper for edgewise and flapwise bending moments are one-half peak-to-peak values taken from steady-state time histories. Figure 8 shows the error in the calculated rotor lift-to-drag ratio as a function of thrust caused by ellipsoids of various thicknesses. The errors are given by $\Delta(L/D) = (L/D) - (L/D)_{\text{exact body}}$. Rotor A was used for these calculations; other parameters are given in Table 2, case 1. Slender body theory gives large errors for the lift-to-drag ratio. The modified theory gave little error. Similar results were calculated for the lift-to-drag ratio of airfoil shaped bodies.

Errors in the oscillatory bending moments were calculated as a function of thrust for various ellipsoids and airfoil shapes. Rotor B was used for these calculations together with the values given in case 1 of Table 2. For ellipsoids with large thickness ratios, modified slender-body theory showed very little error compared with the exact solution for the edgewise bending moment. Slender body theory, on the other hand, showed large errors (20% to 50% for edgewise loads). For a 50%-thick airfoil shape, slender body theory showed an error of about 15% in the edgewise bending moment and the theory without the tail correction still showed an error of about 8% (Fig. 9). Both theories gave errors of less than 5% for 10%- and 30%-thick airfoil shapes.

Figure 10 shows the decrease in lift-to-drag ratio caused by various body shapes. The loss is significant only for large thickness ratios. Rotor A was used together with the parameters in case 1 of Table 2. The ellipsoid results were calculated using the exact solution; the airfoil shaped body results were calculated using the modified

slender body theory with tail correction. Rotor B, together with the parameters of case 1, was used to calculate changes in oscillatory bending loads. In Fig. 11, the blade oscillatory edgewise bending moment is plotted. The edgewise bending load increases for all the body shapes over the range of thrust shown. For the flapwise moment, the trends were similar but the increases were only about 40% of the edgewise load increases.

To determine the cause of the performance change produced by the body, a detailed analysis of the effect of an 80%-thick ellipsoid on rotor A was performed. A small increase in the performance was caused directly by the interference velocity. The loss caused by the profile power and induced power was larger, however, than the gain caused by the interference power. Thus the lift-to-drag ratio decreases. The vertical interference velocity was found to be negative (up) on the front of the disk, and positive (down) on the rear of the disk. Lateral cyclic is needed to cancel the change in flap moment resulting from this 1/rev variation. In general, blade angle of attack α was found to increase inboard and decrease outboard on the front of the disk. On the rear of the rotor disk, α decreased inboard and increased outboard. This angle of attack change produces a change in the blade section drag coefficient, but the pattern of change is different because C_d is a nonlinear function of α. The drag coefficient C_d increased inboard of the region around $\psi = 180°$. On the advancing side, however, C_d increased outboard. The lower values of α on the rear of the disk reduce the drag somewhat. Although α is negative in the tip region in the second quadrant of the rotor disk, the magnitude is such that the C_d is increased on most of the advancing side in the tip region. The profile power coefficient varied similarly to C_d. The rotor blade lift coefficient and induced power change varied similarly to α. The induced power showed a small net increase since the induced velocity generally increases from the front to the back of the rotor disk. The interference power coefficient varied similarly to the interference velocity. The rotor thrust coefficient is higher on the front of the disk (partly because of body effects), so the power increase from the front of the disk is greater than the power loss from the rear of the disk.

To analyze the body effects on the rotor loads, rotor B was used in combination with an 80%-thick ellipsoid. The effect of the body was mainly on the front of the disk from $\psi = 90°$ to $\psi = 270°$. The increase in the edgewise and flapwise bending moments caused by the body was 74% and 26%, respectively, for an 80% ellipsoid and $C_T/\sigma = 0.08$. The change in the edgewise bending moment was positive on the front of the disk, corresponding to a lead motion (Fig. 12). The change in the flapwise bending moment was negative in this region, corresponding to a downward flapping motion. As stated earlier, α was found to increase inboard and decrease outboard on the front of the disk, which explains the behavior of the bending moments. The moduli of the harmonics of the bending moments increased for the first three harmonics. The effect of the body is therefore not just a local phenomenon, but, rather, changes the entire pattern of blade loading.

6. Results: Rotor-Body Aerodynamic Interference

The effects of the body on rotor performance and loads will be examined for cases 2 to 4 of Table 2. Even though the modified slender body theory has been developed here only for axisymmetric bodies at zero angle of attack, a number of practical configurations can be analyzed: a typical full-scale rotor test in the Ames 40- by 80-Foot Wind Tunnel, the Ames small-scale interactional aerodynamics tests, and the future Ames full-scale interactional aerodynamics tests. Modified slender body theory modeled the shapes of the RTA and EE test modules with no significant error in body streamlines (recall that these test modules are modeled with the tails extended to a point, Fig. 3). All of the following results for the influence of the RTA and EE test modules were obtained using the modified slender-body theory with tail correction.

The combination of rotor B and the RTA is a configuration typical of a full-scale wind-tunnel test in the Ames 40- by 80-Foot Wind Tunnel (Fig. 2). Such tests are intended to measure the isolated rotor characteristics. Figures 13-15 were generated under the conditions of case 2 in Table 2. Figure 13 shows the change in angle of attack produced by the RTA for the baseline values of case 2. The advance ratio is 0.4. The increase in the lift-to-drag ratio of rotor B caused by the RTA for various advance ratios was calculated; the increase was negligible ($\Delta(L/D) = 0$ to 0.2; see Fig. 14). The profile and induced power were basically unaffected by the presence of the body; the change in L/D was due almost entirely to the interference power. Figures 15(a) and 15(b) show the increase in the oscillatory edgewise and flapwise bending moments, respectively. The edgewise moments, which were calculated at the 60% radial station, show a 10%-15% increase because of the body. The flapwise bending moments, which were calculated at the 70% radial station, show a 5%-10% increase caused by the RTA. The calculated influence of the RTA on the pitch link loads was negligible (±2%).

To simulate some of the small-scale rotor-body interactional tests conducted at Ames (Fig. 1), the effects of scaled models of the RTA and EE on rotor A were analyzed. Figures 16(a) and 16(b) show the change in angle of attack of the rotor blade caused by the EE for the two longitudinal hub positions in case 3. The baseline values for the advance ratio and the rotor-body vertical separation were used. Moving the hub position aft, as shown in Fig. 16(b), changes the angle-of-attack distribution significantly. The lift-to-drag ratio for rotor A as affected by the RTA and EE was calculated (case 3 of Table 2). Moving the hub aft with respect to the EE nose, at $\mu = 0.3$, created a positive (favorable) change in L/D as compared with the isolated rotor (Fig. 17(a)). Moving the hub position from the forward to the aft position increases the L/D by about 0.4. The change in the total performance is due primarily to the direct interference power. Figures 17(a) and 17(b) show the change in L/D caused by variations in advance ratio, rotor height, and hub position for the EE and RTA, respectively. The decrease in L/D caused by the EE became larger as the advance ratio was increased (Fig. 17(a)). The RTA caused a small increase in L/D at the higher advance ratio (Fig. 17(b)). The variation in rotor height has little effect on the change in L/D for either the EE or the RTA.

Although these calculations are for the small-scale test configurations of Refs. [6]-[8], it is not possible to validate the theory using the rotor performance data of Ref. [6], because of the systematic error now believed to exist in the data. Reference [6] gives data for the rotor alone and with the RTA model. Figure 4 of Ref. [6] shows no trend of the isolated rotor performance with tip-path-plane angle of attack (α_{TPP}), whereas the calculations showed $\Delta(L/D) = 0.5$ to 1.0 for an 8° change in α_{TPP}. Figures 5(a) and 8(b) of Ref. [6] show changes in $\Delta(L/D)$ of the order of 0.5 for the range of advance ratios, hub positions, and rotor-body separation distances investigated; but the calculations show an influence of these parameters that is much less (Fig. 17(b)). Hence, all that can be said is that the calculations support the conclusion that there are systematic errors of the order of 0.5 in the measured rotor L/D.

The combination of the EE and rotor C is a configuration to be used as part of the full-scale interactional tests at Ames (case 4 of Table 2). Figure 18 shows the effect of hub position on the change in L/D caused by the presence of the EE at two advance ratios. The effect of the EE is seen to be very small ($\Delta(L/D) = \pm 0.1$). Figure 19 shows the increase caused by the EE in the oscillatory edgewise bending moment as affected by the hub position at two advance ratios. The moments were calculated at the 50% radial station. The edgewise moment shows an increase of 10%-20% caused by the body for the baseline hub position and a 24%-45% increase for the aft hub position. The corresponding flapwise moment showed a 5%-15% increase because of the body. The effect of the hub position on the flapwise moment was small. Figure 20 shows the time history of the edgewise bending moment for $C_T/\sigma = 0.07$ and $\mu = 0.4$. The effect of the EE is greatest at the front of the rotor disk. The moduli of the harmonics of the loads for this case are increased for the first four harmonics. The calculated effect of the EE on the pitch link loads was small (a 4%-8% increase).

7. Computation Efficiency

The computational efficiency of modified slender body theory can be assessed by comparing the time required for the body analysis and the time needed for the rotor portion of the analysis. The amount of time required for the body analyses depended on the frequency with which the body velocities were updated within CAMRAD. Two approaches were used to estimate the computational efficiency: 1) update body velocities (over the entire rotor disk) once per wake iteration, and 2) update body velocities once per control change in the trim iteration. One wake iteration involves typically 5 to 15 steps of control changes (see Fig. 4). Note that the rotor analysis begins with a uniform inflow solution, then proceeds to a nonuniform inflow with prescribed wake geometry, and then to a nonuniform inflow with free-wake geometry (see Ref. [5]).

Approach (2) can be considered a fully converged body velocity calculation, since the rotor motion, and hence the rotor position relative to the body, changes very little during the final steps of the trim iteration (Fig. 4). The wake influence coefficient calculation (as a percentage of the time required for the entire job) requires

35%-40% using approach (1) and 15%-25% using approach (2). The body velocity calculation requires 5%-10% using (1) and 40%-70% using (2). Approach (2) required a factor of 10-20 more updates of the body-induced velocities than approach (1).

Regarding accuracy, approach (1) with two wake iterations gave less than a 1% difference in performance and loads compared with approach (2). Also, approach (1) with two iterations required about the same total time, or even less, than approach (2) with one wake iteration. For an optimally accurate and computationally efficient solution, a more complex method of determining when to update the body-induced velocities is needed. A satisfactory method is to update the velocities when the change in rotor position relative to the body exceeds some criterion. Updating the body velocities three to five times at the beginning of the trim iteration would be sufficient.

If the body velocities are updated three to five times per wake iteration in the rotor solution, then calculating the velocities using modified slender body theory will require 10%-20% of the time required for a complete rotor solution. If a panel method is used, however, the time required to calculate the velocities will be two to six times that required for a complete rotor solution, depending on the complexity of the panel code. (Although a more efficient panel code could be constructed for the case of an axisymmetric body at zero angle of attack, the above comparison of computation time refers to the more general problem.)

8. Conclusions

Modified slender body theory was used to assess body-induced effects on rotor behavior. The effects of several body shapes on three different rotors were studied. The wide range of configurations covered was made possible by the computational efficiency of the body model. Conclusions drawn from this study are listed below.

1) Moderately thick ellipsoids are modeled well by modified slender body theory. The streamlines of body shapes with pointed ends can be closely matched by the modified slender body theory with tail correction, but a trial and error procedure is necessary to find the two free parameters in the tail correction procedure.

2) In assessing the effects on the rotor of simple body shapes, slender body theory produced significant errors (relative to the exact solution) except for thin shapes, whereas the modified slender body theory was accurate for moderately thick bodies.

3) Since the body-induced effects depend on the detailed aerodynamic environment of the rotor blade, nonuniform inflow induced velocity calculations must be used in the rotor analysis. A free wake model produced essentially the same results as a prescribed wake geometry model, implying that the neglect of body-induced distortions of the wake geometry is acceptable.

4) The calculated influence of the body on the rotor performance was generally small for the cases considered here. The direct interference power can be positive or negative, depending on the body configuration. The interference power is typically not zero, even for cases with exact fore-aft symmetry of the interference velocity, as a result of the asymmetry of the rotor loading distribution. For the cases considered here, the profile power and induced power were always increased by the presence of the body. The profile power increase was generally greater than the induced power increase. The net performance change caused by the body could be favorable or unfavorable, depending on the sign of the direct interference power and its magnitude relative to the profile power change.

5) The calculated oscillatory blade bending moments were always increased by the body for the cases considered here. The edgewise bending moment changes were larger than the flapwise bending moment changes. In some cases, the loads were increased by a significant fraction of the isolated rotor loads. The interference effects were due to the general changes in the rotor flow pattern, rather than to localized effects of the body. The influence of the body on the blade loads occurred primarily on the front of the rotor disk. No significant effects on pitch link loads were found.

6) For the case of a typical full-scale rotor test in the 40- by 80-Foot Wind Tunnel, negligible effects of the Rotor Test Apparatus (RTA) on the rotor performance and pitch link loads were calculated. Only small increases in the blade bending moments were found. Hence, such a test does produce essentially isolated rotor behavior.

7) For the case of the Ames small-scale aerodynamic interference tests, a performance change of about $\Delta(L/D) = 0.2$ due to the Easter Egg (EE) body shape was calculated. A 6% performance change ($\Delta(L/D) = 0.4$) was predicted for the two body longitudinal positions tested. The corresponding influence of the model RTA body shape was small. The calculated influences of the rotor-body vertical separation was small for both body shapes.

8) For the case of the Ames full-scale aerodynamic interference tests, it is predicted that the EE body will produce negligible performance changes. The oscillatory edgewise bending moments will be 10%-20% higher than for the isolated rotor with the EE at the baseline position. If the EE body were shifted forward, the loads would be 25%-45% higher than for the isolated rotor. Smaller effects are predicted for the influence of the body on the flapwise bending moment.

9) The computational efficiency of the body model is one or two orders of magnitude better than that of a typical potential flow panel code. The body analysis using the modified slender body theory required only 10%-20% of the computation time required for the rotor analysis.

References

1) P. F. Sheridan and R. P. Smith, Interactional Aerodynamics — A New Challenge to Helicopter Technology, J. Am. Helicopter Soc., Vol. 25, No. 1, 1980.

2) P. G. Wilby, G. Young, and J. Grant, An Investigation of the Influence of Fuselage Flow Field on Rotor Loads and the Effects of Vehicle Configuration, Vertica, Vol. 3, No. 2, 1979.

3) C. E. Freeman and J. C. Wilson, Rotor-Body Interference (ROBIN) — Analysis and Test, 36th Annual Forum of the American Helicopter Society, Washington, D.C., May 1980.

4) D. R. Clark and B. Maskew, Calculation of Rotor/Airframe Interference for Realistic Configurations, European Rotorcraft and Powered Lift Aircraft Forum, Aix-en-Provence, France, Sept. 1982.

5) W. Johnson, Development of a Comprehensive Analysis for Rotorcraft, Vertica, Vol. 5, Nos. 2 and 3, 1981.

6) M. D. Betzina and P. Shinoda, Aerodynamic Interactions Between a 1/6-Scale Helicopter Rotor and a Body of Revolution, NASA TM-84247, 1982.

7) M. D. Betzina, C. A. Smith, and P. Shinoda, Rotor/Body Aerodynamic Interactions, NASA TM-85844, 1983.

8) C. A. Smith and M. D. Betzina, A Study of the Aerodynamic Interaction Between a Main Rotor and a Fuselage, 39th Annual Forum of the American Helicopter Society, St. Louis, Mo., May 1983.

9) T. Trept, A 0.15-Scale Study of Configuration Effects on the Aerodynamic Interaction Between Main Rotor and Fuselage, NASA CR-166577, 1984.

10) H. Huber and G. Polz, Studies on Blade-to-Blade and Rotor-Fuselage-Tail Interference, AGARD Conference Proceedings No. 334, London, May 1982.

11) A. J. Landgrebe, R. C. Moffitt, and D. R. Clark, Aerodynamic Technology for Advance Rotorcraft, J. Am. Helicopter Soc., Vol. 22, No. 3, July 1977.

12) T. W. Sheehy, A Simplified Approach to Generalized Helicopter Configuration Modeling and the Prediction of Fuselage Surface Pressures, J. Am. Helicopter Soc., Vol. 21, No. 1, Jan. 1976.

13) D. Jepson, R. Moffitt, K. Hilzinger, and J. Bissell, Analysis and Correlation of Test Data from an Advanced Technology Rotor System, NASA CR-3714, 1983.

14) P. F. Sheridan, Interactional Aerodynamics of the Single Rotor Helicopter Configuration, U.S. Army Research and Technology Laboratories, TR 78-23, Sept. 1978.

15) J. C. Wilson and R. E. Mineck, Wind-Tunnel Investigation of Helicopter-Rotor Wake Effects on Three Helicopter Fuselage Models, NASA TM X-3185, 1975.

16) G. K. Yamauchi and W. Johnson, Development and Application of an Analysis of Axisymmetric Body Effects on Helicopter Rotor Aerodynamics Using Modified Slender Body Theory, NASA TM-85934, 1984.

17) N. Curle and H. J. Davies, Modern Fluid Dynamics, D. Van Nostrand Company, Ltd., Canada, 1968.

18) B. Thwaites, Incompressible Aerodynamics, Clarendon Press, Oxford, 1960.

19) W. F. Durand, ed., Aerodynamic Theory, Vol. I, Julius Springer, Berlin, 1934.

TABLE 1.- ROTOR TYPES USED IN ANALYSIS

Type	Rotor A (teetering)	Rotor B (articulated)	Rotor C (articulated)
Number of blades	2	4	4
Radius, m	1.12	6.71	7.01
Solidity ratio	0.0651	0.0748	0.0705
Twist, deg	-10	-10 (nonlinear)	-14 (nonlinear)
Lock number	3.44	9.08	7.19
Tip Mach number	0.60	0.60	0.70

TABLE 2.- SUMMARY OF CASES (BASELINE VALUES)

	Case 1		Case 2	Case 3		Case 4
Rotor	A, B		B	A		C
μ	0.4		0.4	0.3		0.3
α_S	0		0	0		-4
α_{TPP}	-4		0	0		-4
Body	Ellipsoids	NACA 00xx	RTA	Model RTA	Model EE	EE
ℓ/R	1.0	1.0	1.5152	1.515	1.021	0.942
$2t^a$	0.8	0.3	0.1749	0.1749	0.3074	0.3074
$(x/\ell)_{hub}{}^b$	0.5	0.25	0.295	0.295	0.199	0.206
$(\Delta z/\ell)_{hub}{}^c$	0.1	0.1	0.088	0.053	0.070	0.85
$(y/\ell)_{hub}{}^d$	0	0	0	0	0	0

[a]Thickness ratio. [b]Relative to nose. [c]Relative to top of body. [d]Relative to centerline.

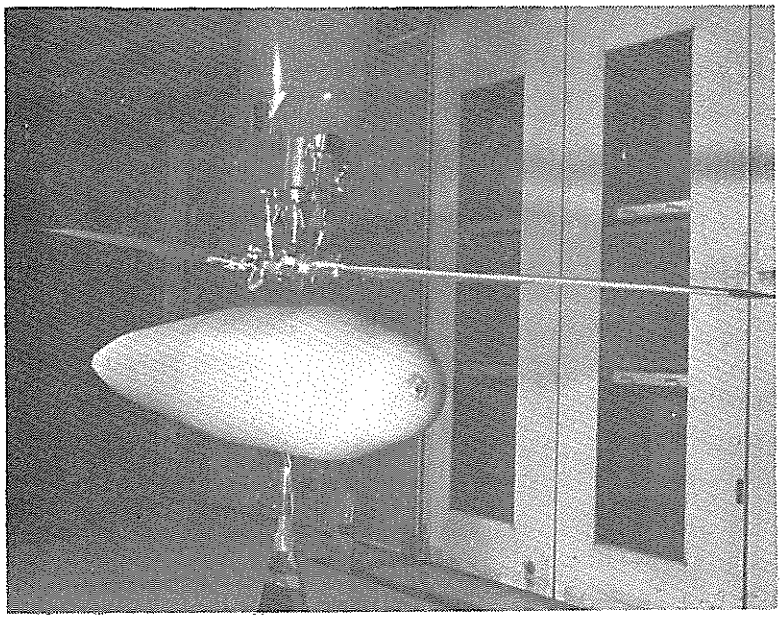

(a) Rotor Test Apparatus test module.

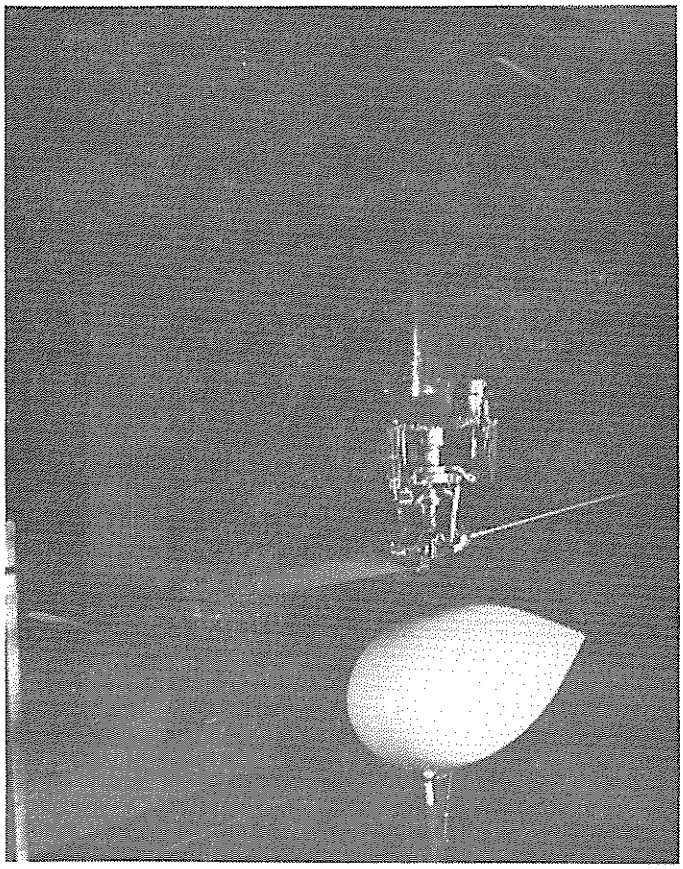

(b) Easter Egg test module.

Figure 1. Model rotor and 1/6-scale test module in the Ames 7- by 10-Foot Wind Tunnel for rotor/body aerodynamic interference tests.

Figure 2. Typical full scale rotor test in the Ames 40- by 80-Foot Wind Tunnel (on the Rotor Test Apparatus).

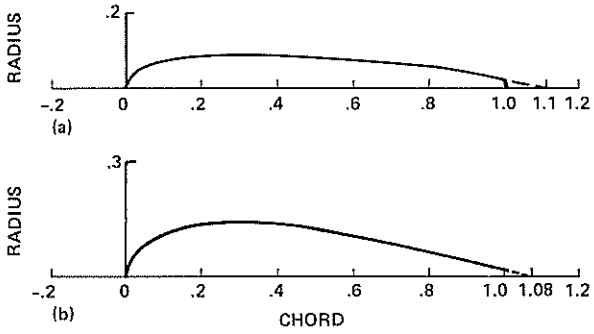

Figure 3. Body streamlines of test modules (dashed lines are tail extensions). (a) Rotor Test Apparatus. (b) Easter Egg.

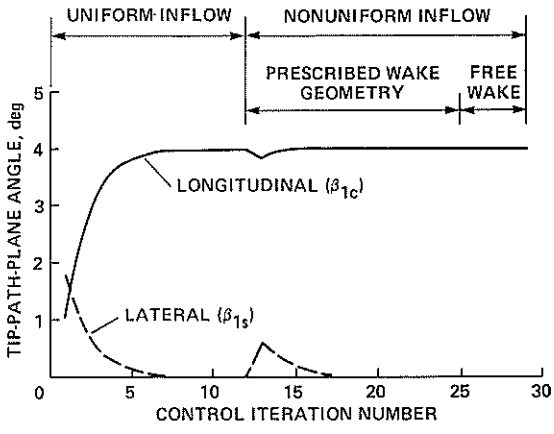

Figure 4. Convergence of rotor blade position during typical trim iteration.

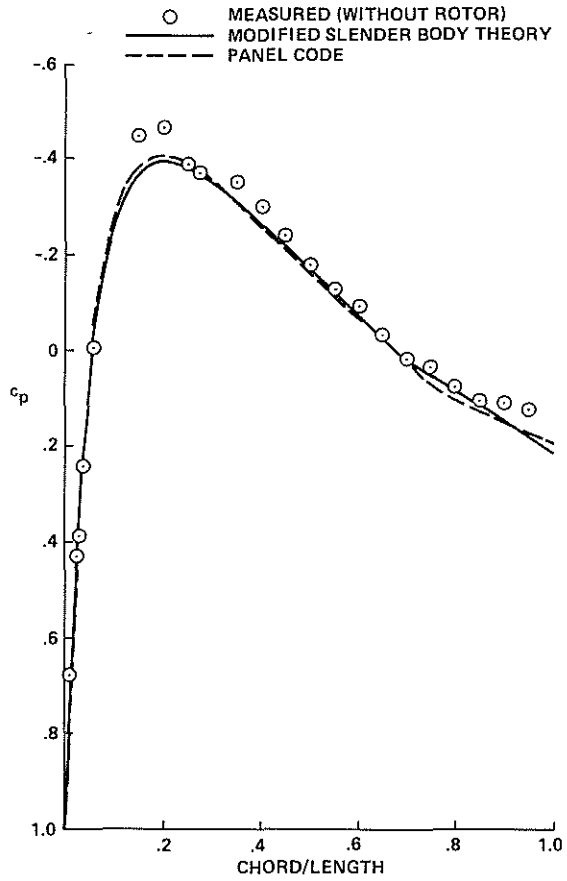

Figure 5. Pressure distribution on an isolated Easter Egg at zero angle of attack, compared with measured data (reference 8) and with panel code calculations (reference 8).

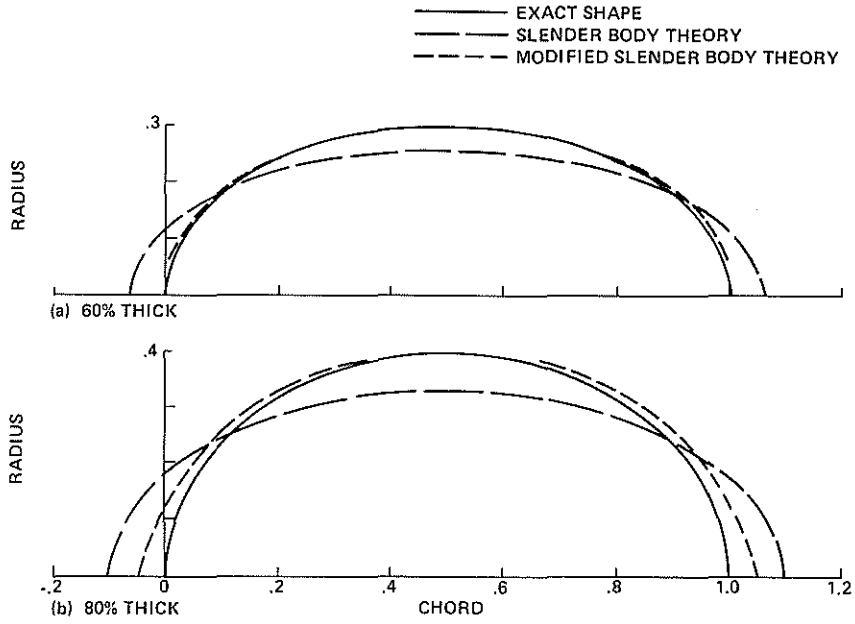

Figure 6. Body streamlines for ellipsoids, comparing exact, slender body, and modified slender body theories.

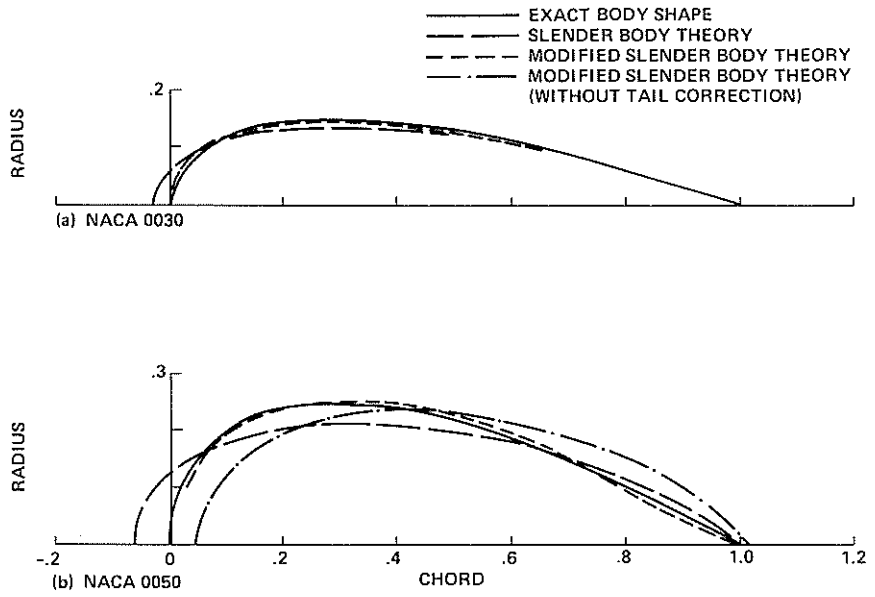

Figure 7. Body streamlines for axisymmetric bodies with NACA four-digit airfoil thickness distribution.

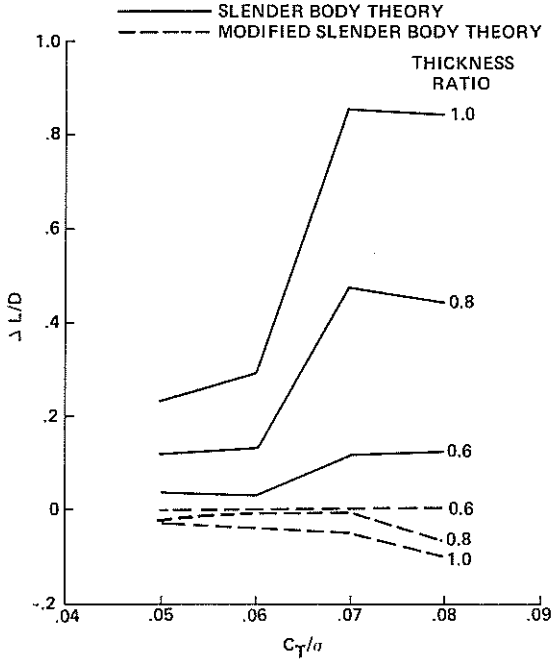

Figure 8. Error in lift-to-drag ratio for rotor A in combination with ellipsoids of various thicknesses (case 1).

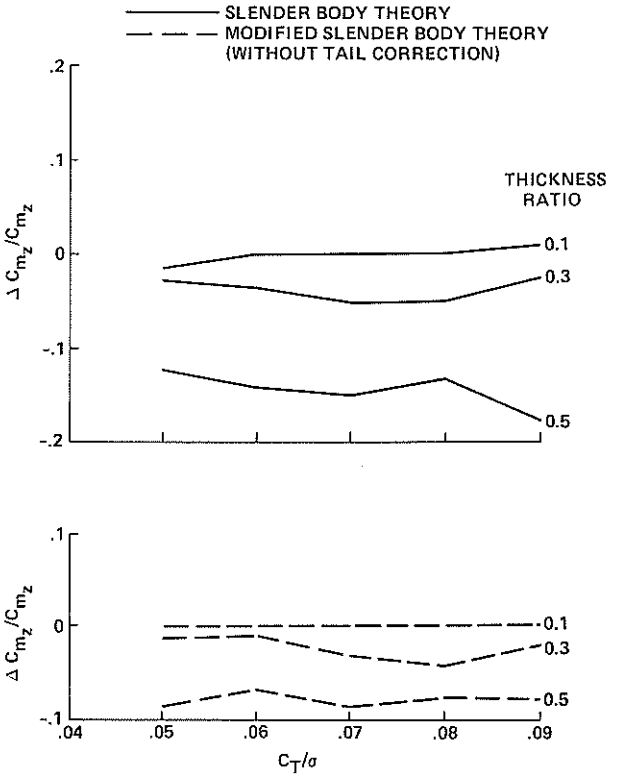

Figure 9. Error in oscillatory edgewise bending loads at 0.6R for rotor B in combination with airfoil-shaped bodies of various thicknesses (case 1).

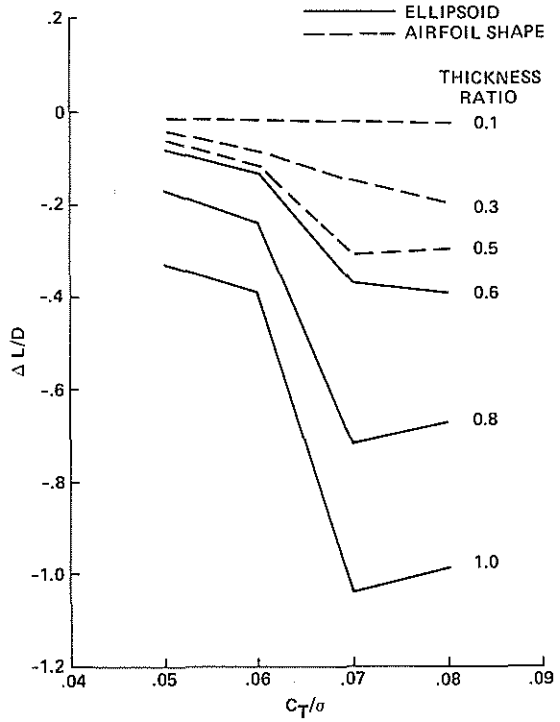

Figure 10. Change in lift-to-drag ratio for rotor A due to bodies of various thicknesses (case 1).

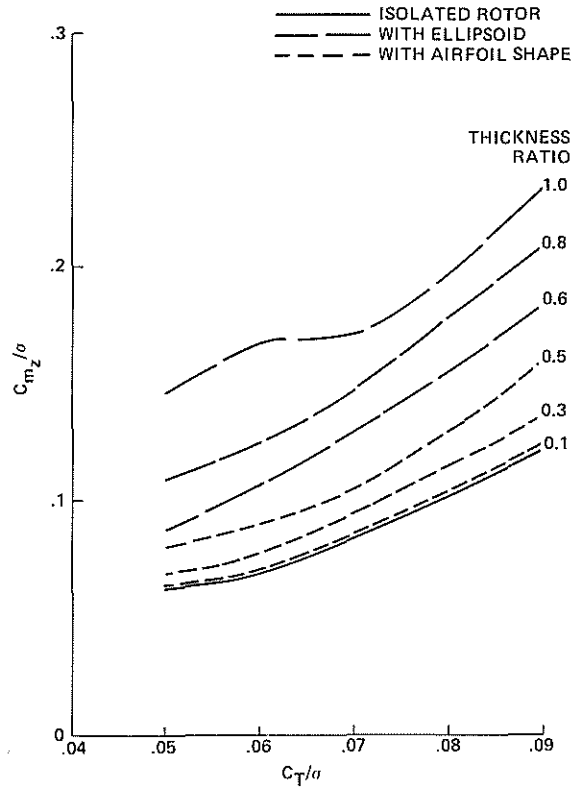

Figure 11. Oscillatory edgewise bending loads at 0.6R for rotor B due to bodies of various thicknesses (case 1).

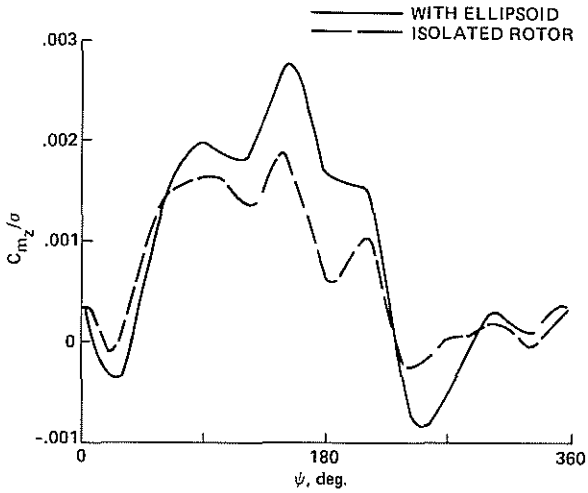

Figure 12. Edgewise bending moment at 0.6R for rotor B at C_T/σ = 0.08 with an 80%-thick ellipsoid (case 1).

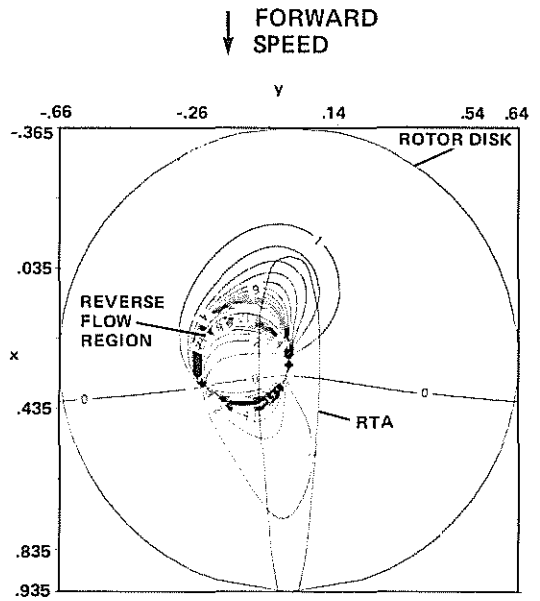

Figure 13. Plot of rotor blade angle-of-attack change (deg) due to the Rotor Test Apparatus in the plane of the rotor disk, μ = 0.4 (case 2).

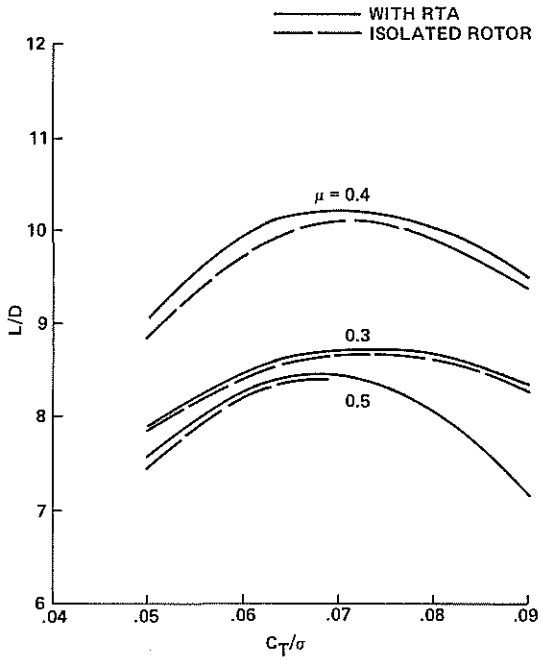

Figure 14. Lift-to-drag ratio for rotor B and Rotor Test Apparatus configuration for several advance ratios (case 2).

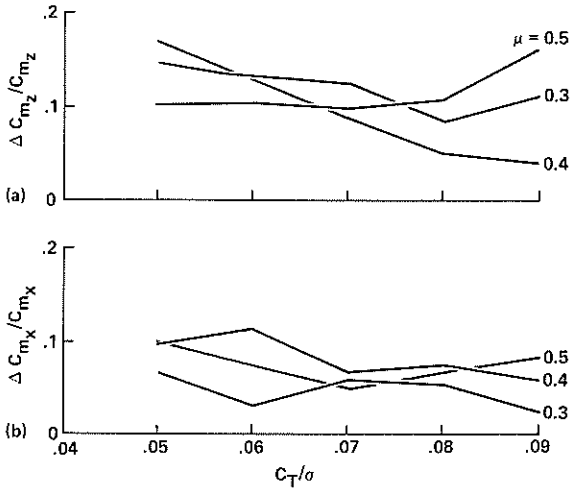

Figure 15. Increase in oscillatory bending moments for rotor B due to the Rotor Test Apparatus (case 2). (a) Oscillatory edgewise bending moment at 0.6R. (b) Oscillatory flapwise bending moment at 0.7R.

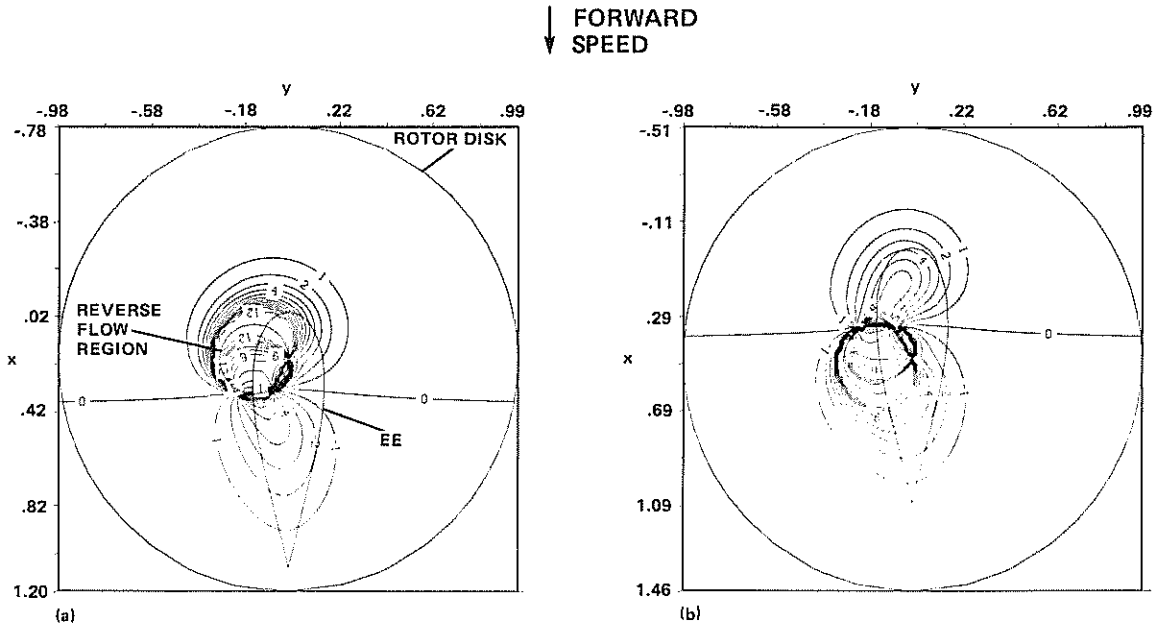

(a) $(x/\ell)_{HUB}$ = 0.199. (b) $(x/\ell)_{HUB}$ = 0.471.

Figure 16. Plot of rotor blade angle-of-attack change (deg) due to the Easter Egg in plane of the rotor disk, μ = 0.3 (case 3).

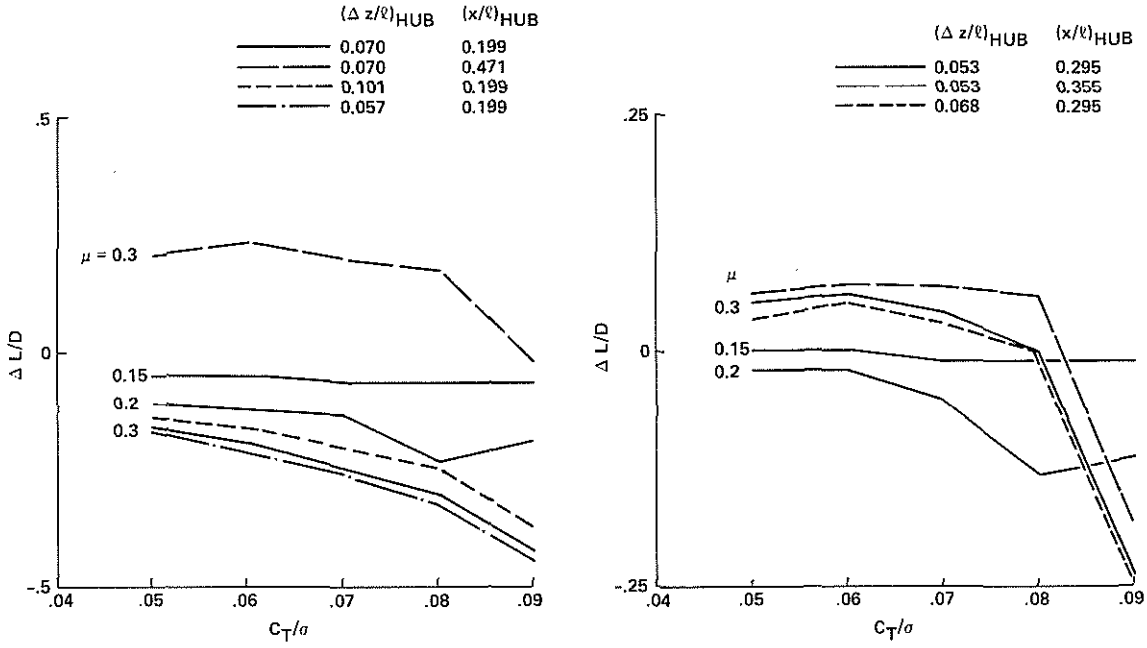

(a) Easter Egg. (b) Rotor Test Apparatus.

Figure 17. Effect of changing advance ratio, longitudinal hub position, and rotor-body vertical separation on the change in lift-to-drag ratio of rotor A due to the test modules (case 3).

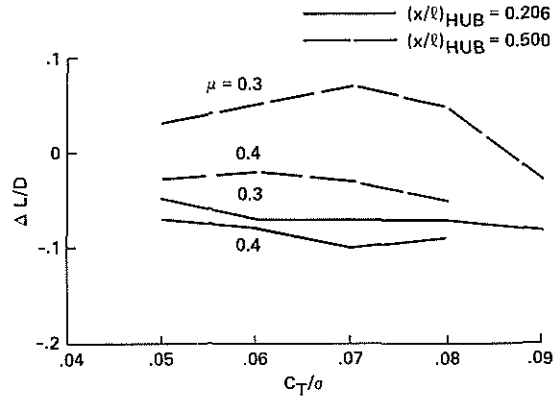

Figure 18. Effect of hub position on the change in lift-to-drag ratio for rotor C due to the Easter Egg for two advance ratios (case 4).

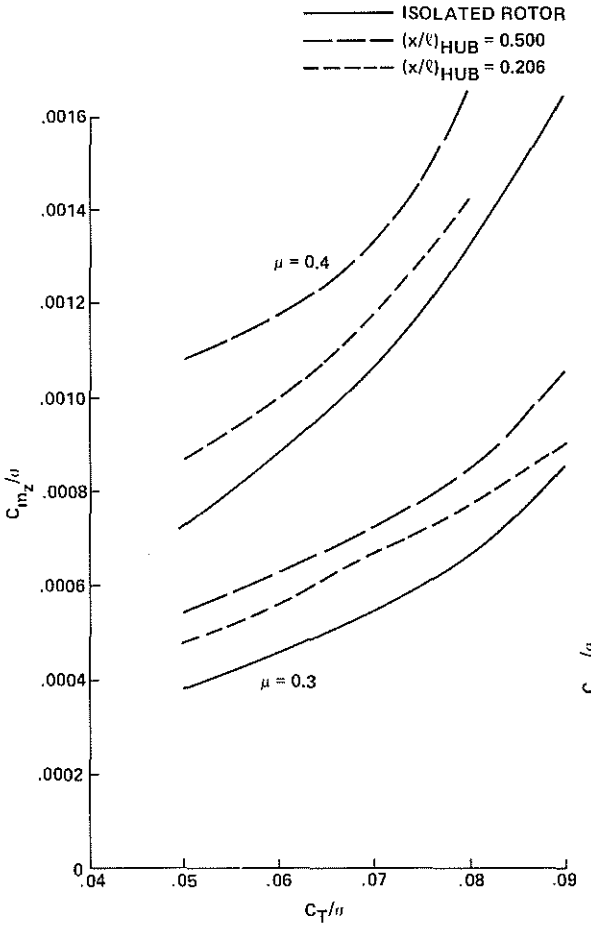

Figure 19. Effect of hub position on the oscillatory edgewise bending moments at 0.5R for rotor C due to the Easter Egg for two advance ratios (case 4).

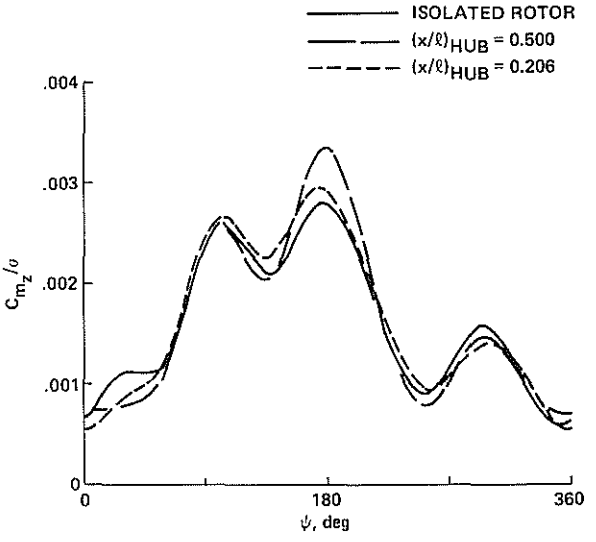

Figure 20. Effect of hub position on the edgewise bending moment at 0.5R for rotor C and Easter Egg configuration at $C_T/\sigma = 0.07$ and $\mu = 0.4$ (case 4).